ACS OMEGA

http://pubs.acs.org/journal/acsodf

Article

Optoelectronic Properties Prediction of Lead-Free Methylammonium Alkaline-Earth Perovskite Based on DFT Calculations

Chih Shan Tan* and Chung Chi Yang

Cite This: *ACS Omega* 2022, 7, 16204−16210

Read Online

ACCESS | Metrics & More | Article Recommendations | Supporting Information

ABSTRACT: Dynamical stability plays an essential role in phase transition and structure, and it could be a fundamental method of discovering new lead-free perovskite materials. The perovskite materials are well-known for their excellent optoelectronic properties, but the lead element inside could be a hindrance to future development. This research is trying to predict the promising cation candidates in the high-temperature application for lead-free perovskite materials from the replacement of lead in $MAPbCl_3$ (MA = methylammonium) with alkaline-earth cations. The alkaline-earth cations are of a stable positive divalent sort, which is the same as Pb, and most of them are abundant in nature. Therefore, by improving the dynamical stability, the Mg^{2+}, Ca^{2+}, and Sr^{2+} cations replacement of lead ions could stabilize the perovskite structure by decreasing the imaginary part of phonon density of states. Finally, the density functional theory results show that the $MACaCl_3$ could be a dynamic stable lead-free methylammonium perovskite material with an ultrawide band gap (5.96 eV).

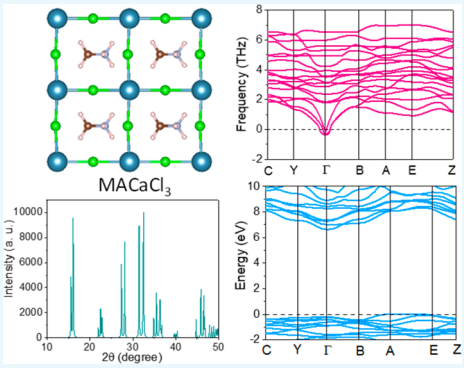

INTRODUCTION

Environmentally friendly ultrawide band-gap materials need to be developed for the next-generation ultraviolet C luminescence applications in disinfection, biosensing, and environmental monitoring.[1−5] The organic−inorganic perovskite materials could be potential candidates for ultrawide band-gap optoelectronics due to their excellent carrier mobility and lifetime, high flexibility, and low formation temperature.[6−9] However, there is a lack of high external quantum efficiency (EQE) material for ultraviolet C devices (4.42−12.4 eV), and a new type of organic−inorganic perovskite could offer a solution. The density functional theory (DFT) calculation can determine the electronic structure and phonon dispersion diagram for the electrical and dynamic stability property of new organic−inorganic perovskite structures and determine the possibility for device application.[10−12] Previously, the DFT was typical for explaining experimental results by calculating the band structure.[13−21] However, the DFT is already used to predict new materials,[22−25] and the guidance of a DFT calculation can shorten the development timing and cost. Thus, this research conducts the DFT calculation with the GGA-PBE[26] and sx-LDA[27,28] functionals for new types of lead-free methylammonium (MA, CH_3NH_3) alkaline-earth perovskite searching. Furthermore, the geometry optimization calculation by the GGA-PBE functional could be a suitable method for moving the atoms and molecules to get the most stable structure with the lowest possible ground-state energy.

The perovskite structure ABX_3 has a wide range of tolerance factors (0.8−1) for keeping the same cubic structure with different elements inside.[29−32] Previously, the DFT calculation was conducted for discussing the structure and electronic structure issue of the lead cation replacement with the alkaline-earth cations within $MAPbI_3$.[33] However, the dynamic stability and possible electrical conductivity of the alkaline-earth perovskites are yet to be mentioned. Thus, this research is focused on the dynamic stability, electrical conductivity, and carrier mobility of the methylammonium alkaline-earth perovskite. $MAPbCl_3$ has experimental wide band-gap values such as 2.88 eV (single crystal)[34] with a relatively stable perovskite structure with space group $Pm\bar{3}m$. However, the DFT calculation of $MAPbCl_3$ by the sx-LDA functional can offer a 2.74 eV value, which is closer to the experimental value of 2.88 eV. Therefore, this research uses the sx-LDA functional for the lead-free perovskite estimation. On the basis of the wide band-gap property of $MAPbCl_3$, the lead ion will be replaced by alkaline-earth ions and form new perovskite structures. The calculation results demonstrate that the alkaline-earth cations, such as Mg^{2+}, Ca^{2+}, and Sr^{2+}, might be potential candidates for

Received: March 21, 2022
Accepted: March 30, 2022
Published: April 25, 2022

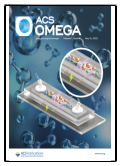

https://doi.org/10.1021/acsomega.2c01695
ACS Omega 2022, 7, 16204−16210

methylammonium lead-free perovskites due to the better dynamic stability and wider band gap of methylammonium lead perovskite.

RESULTS AND DISCUSSION

Figure 1 shows the $MAPbCl_3$ and the alkaline-earth cations (Be^{2+}, Mg^{2+}, Ca^{2+}, Sr^{2+}, and Ba^{2+}) that replace lead cation

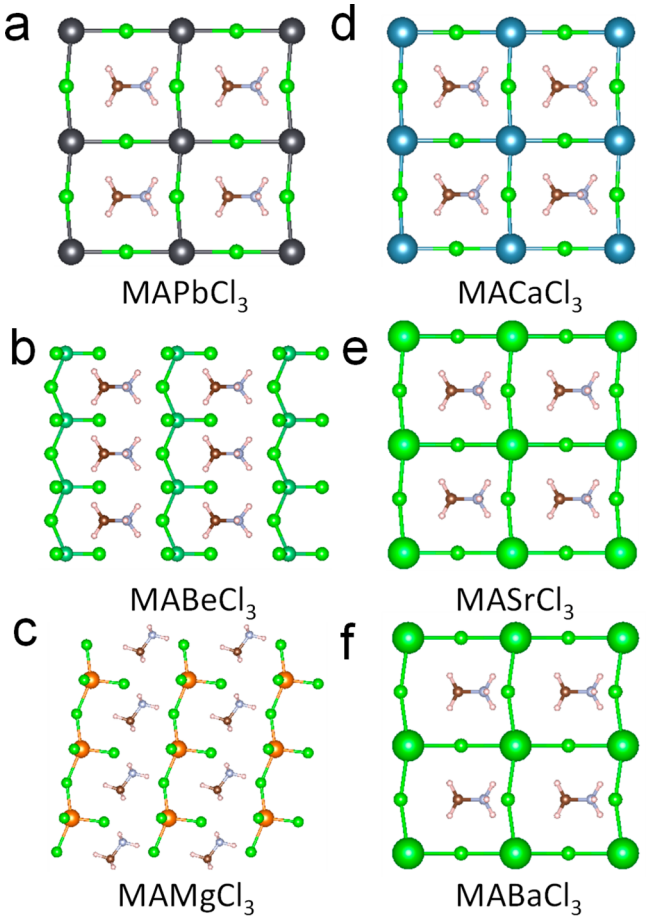

Figure 1. Structures of $MAPbCl_3$ and the alkaline-earth cations replace lead-free perovskite structures. (a) The original $MAPbCl_3$ structure ($Pm\bar{3}m$). (b) Be^{2+} replaced Pb^{2+}, the $MABeCl_3$ structure. (c) Mg^{2+} replaced Pb^{2+}, the $MAMgCl_3$ structure. (d) Ca^{2+} replaced Pb^{2+}, the $MACaCl_3$ structure. (e) Sr^{2+} replaced Pb^{2+}, the $MASrCl_3$ structure. (f) Ba^{2+} replaced Pb^{2+}, the $MABaCl_3$ structure.

structures, and the precise atom positions and structure parameters are listed in Table S1. The structures after the structure optimization are shown in Figure 1a–f. Those alkaline-earth cation lead-free structures, after structure optimization, are listed with their parameters in Table S1. Indeed, the $MABeCl_3$ and $MAMgCl_3$ structures are distorted toward two-dimensional perovskites, as shown in Figure 1b,c. The lattice distortion is huge within the $MABeCl_3$, 12.0%, −33.5%, and 9.1%, in the *a*-, *b*-, and *c*-axis directions, respectively. Therefore, the lattice volume of $MABeCl_3$ undergoes a −19.6% change from the original $MAPbCl_3$ structure and makes $MABeCl_3$ unable to sustain the original structure. $MAMgCl_3$ has the same distortion issue with 13.3% of the crystal volume, caused by three nonequal crystal axes. The other alkaline ion replacements made the lattice volume in $MAPbCl_3$ change by −10.8%, 0.6%, and 14.7% for Ca^{2+}, Sr^{2+}, and Ba^{2+}, respectively. All the structure optimization results about the atom positions within the structures are listed in Table S2. In fact, the lattice distortions are not small, but the calculation results demonstrate that $MACaCl_3$, $MASrCl_3$, and $MABaCl_3$ could still maintain perovskite as the P_m space group. As for the tolerance factors (Goldschmidt factors) shown in Table 1, they are better to be 0.8−1 to sustain the perovskite structure and have better stability between 0.94 and 0.98. In Table 1, $MABeCl_3$ and $MAMgCl_3$ have the Goldschmidt factors higher than 1, making it hard to keep the perovskite structure, and $MABaCl_3$, $MAPbCl_3$, and $MASrCl_3$ can sustain the structure with normal stability. Finally, $MACaCl_3$ gets the most stable Goldschmidt factor of 0.96, probably having better stability for future device applications.

The phonon dispersion in the crystal has often been studied to determine the dynamic stability of a structure, and a stable structure normally only has positive vibration states within phonon dispersion. Because the crystal bonding energy will lose to negative vibration states within the structure's phonon vibration, not only will the atomic bonding be broken but also the structure will disappear, finally. Also, the phonon dispersion diagram shows that the positive and negative vibration states can be regarded as real and imaginary states. Thus, the crystals that have negative frequencies might be unstable. The phonon dispersion and phonon density of states (DOSs) diagrams are shown in Figure 2a–f for $MAPbCl_3$, $MABeCl_3$, $MAMgCl_3$, $MACaCl_3$, $MASrCl_3$, and $MABaCl_3$, respectively. In Figure 2a, the $MAPbCl_3$ has negative frequencies phonon dispersion, and the imaginary part of the whole phonon DOS is 1.78%, as shown in Table 1. $MAPbCl_3$ has poor long-term stability under room-temperate ambient conditions. $MAMgCl_3$, $MACaCl_3$, and $MASrCl_3$ have smaller negative frequencies phonon dispersion parts, which means that replacing Mg^{2+}, Ca^{2+}, and Sr^{2+} can decrease the imaginary part of a phonon DOS from 1.78% to 1.30%, 0%, and 0.54%, as shown in Table 1. Therefore, Mg^{2+}, Ca^{2+}, and Sr^{2+} might make the perovskite structure more dynamically stable in future lead-free perovskite devices. The energy of the system in each crystal is listed in Table 1 by calculating under 0 K, and the phonon dispersion of a crystal offers a reliable stability reference. For example, $MACaCl_3$ has 0% of the imaginary part of a phonon DOS, which means it is

Table 1. Metal Ion Radius, the Energy of the System (E_0), the Imaginary Part of Phonon Density of State (DOS), Debye Temperature (θ_D), and Goldschmidt Factor of Different Structures

	metal ion radius (Å)	Goldschmidt factor	energy of the system, E_0 (eV)	imaginary part of phonon DOS (%)	Debye temperature, θ_D (K)
$MAPbCl_3$	1.33	0.90	−64.25	1.78	102
$MABeCl_3$	0.59	1.20	−54.92	3.94	178
$MAMgCl_3$	0.86	1.07	−53.95	1.30	131
$MACaCl_3$	1.14	0.96	−56.33	0	233
$MASrCl_3$	1.32	0.91	−56.24	0.54	115
$MABaCl_3$	1.49	0.86	−56.47	5.40	108

https://doi.org/10.1021/acsomega.2c01695
ACS Omega 2022, 7, 16204−16210

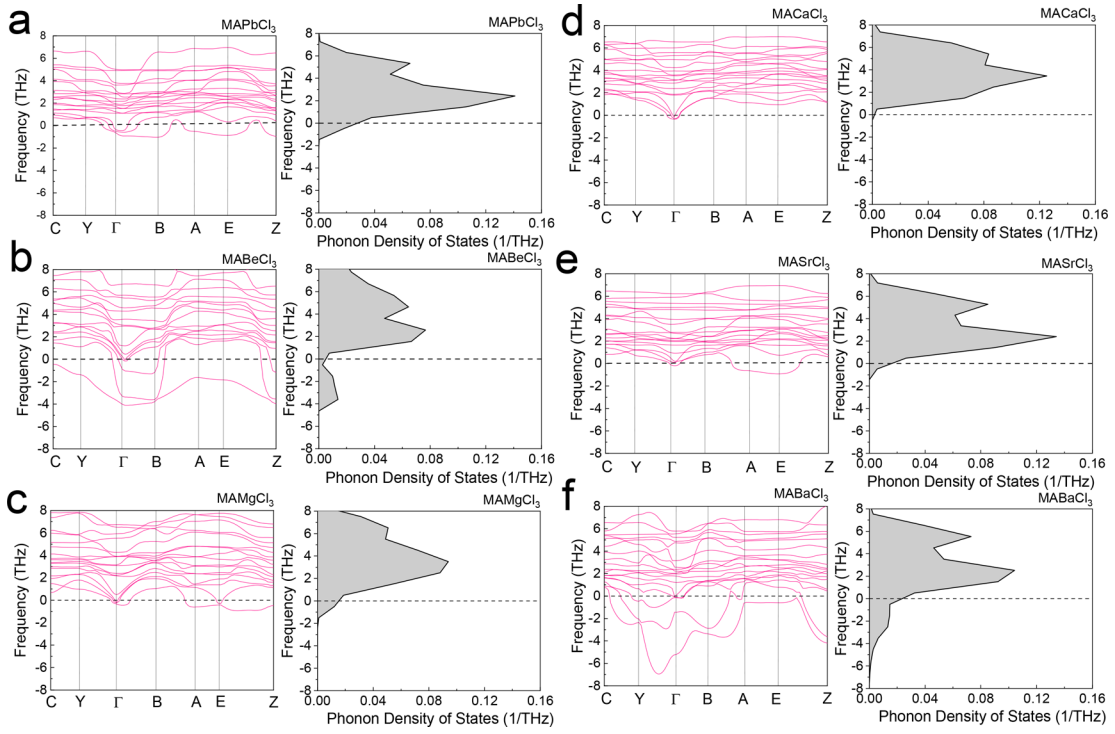

Figure 2. Phonon dispersion diagrams and phonon DOSs of (a) $MAPbCl_3$, (b) $MABeCl_3$, (c) $MAMgCl_3$, (d) $MACaCl_3$, (e) $MASrCl_3$, and (f) $MABaCl_3$ (PBE-GGA).

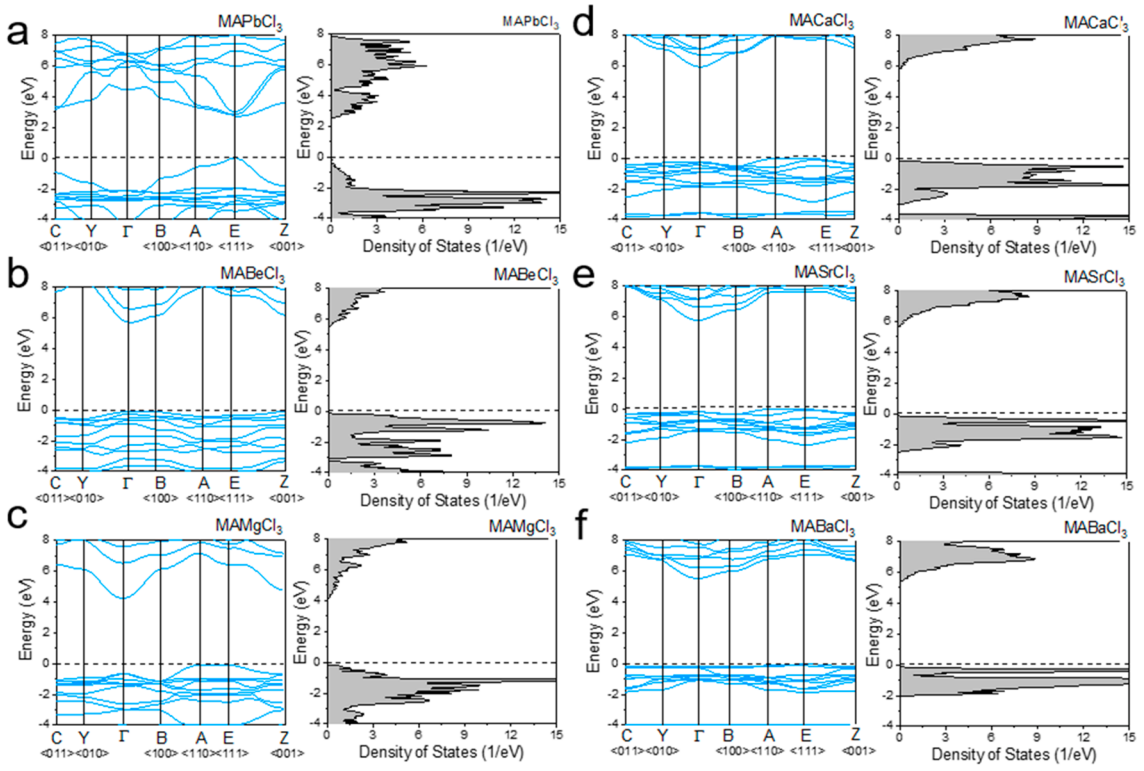

Figure 3. Electronic band structures and DOSs of (a) $MAPbCl_3$, (b) $MABeCl_3$, (c) $MAMgCl_3$, (d) $MACaCl_3$, (e) $MASrCl_3$, and (f) $MABaCl_3$ (sx-LDA).

more stable than others and suitable for a future dynamically stable ultrawide band-gap lead-free perovskite device.

The formation temperature of an unknown lead-free methylammonium perovskite could guide material synthesis and device fabrication. Further, a thermodynamic calculation can offer the Debye temperature value and the higher Debye temperature (θ_D) of a crystal that accompanies a higher melting temperature and higher formation temperature. Therefore, the temperature-dependent heat capacity, entropy, and Helmholtz free energy are shown in Figure S1a−c (0−500 K) and Figure

https://doi.org/10.1021/acsomega.2c01695
ACS Omega 2022, 7, 16204−16210

S1d−f (0−3000 K). According to the Debye model, the Debye temperature (listed in Table 1) could be obtained by the linear relationship of the heat capacity. Hence, the $MAMgCl_3$ (θ_D = 131 K), $MACaCl_3$ (θ_D = 233 K), and $MASrCl_3$ (θ_D = 115 K) structures might need higher formation temperatures than $MAPbCl_3$ (θ_D = 102 K) for a future experiment due to the higher Debye temperatures.

The electrical band structures of the $MAPbCl_3$ and the alkaline-earth cations (Be^{2+}, Mg^{2+}, Ca^{2+}, Sr^{2+}, and Ba^{2+}) replace lead structures in Figure 3a−f, with the Fermi levels all set as zero. The critical points of the Brillouin zone within the $Pm\bar{3}m$ space group of $MAPbCl_3$ and alkaline-earth cation-replaced structures are E (111), A (110), Y (010), Z (001), B (100), Γ (000), and C (011), and Γ is the center point of the Brillouin zone. In Figure 3, the results are different DFT calculation results using sx-LDA, and the PBE-GGA results are shown in Figure S2. In Figure 3a, the valence band maximum (VB_{max}) and conduction band minimum (CB_{min}) of $MAPbCl_3$ are −0.2 and 2.54 eV on the E (111) critical points. The direct band gap with proper bandwidth makes it a suitable material for a green light optoelectronic device. As for the replaced ones, in Figure 3b−f, their bandwidths are 5.71, 4.29, 5.96, 5.8, and 5.58 eV. And, $MABeCl_3$ is the only direct band-gap lead-free methylammonium alkaline-earth perovskite.

In Table 2, except for $MAPbCl_3$ (453 nm), all methylammonium alkaline-earth perovskites have the ultraviolet C range (100−280 nm) properties. In Table 2, the band gap of $MAPbCl_3$ is 2.74 eV with 5.1% deviation from the experimental results by 2.88 eV (single crystal).[34] Therefore, the DFT band gap calculation using the sx-LDA functional has a low deviation (5.1%) with the thin-film experimental result and could be used to predict the band gaps of methylammonium perovskites in which lead was replaced with alkaline-earth cations. Furthermore, $MAMgCl_3$ has the lowest band gap (4.29 eV), while the other materials have band gaps that are each more than 5 eV. This might be caused by the different ion radii and the electron orbits. Indeed, the Goldschmidt factor of $MAMgCl_3$ is slightly larger than 1, at 1.07, and this might be the reason for the influence of the orbital and band gap. According to different Goldschmidt factor values, structure variations might change the band gaps.

Table 2. Semiconductor Band Information of $MAPbCl_3$, $MABeCl_3$, $MAMgCl_3$, $MACaCl_3$, $MASrCl_3$, and $MABaCl_3$

sx-LDA	VB_{max} (eV)	CB_{min} (eV)	carrier transfer (VB_{max} to CB_{min})	band gap (eV/nm)
$MAPbCl_3$	−0.20	2.54	(111) to (111)	2.74/453
$MABeCl_3$	−0.21	5.48	(000) to (000)	5.71/217
$MAMgCl_3$	−0.22	4.06	(111) to (000)	4.29/289
$MACaCl_3$	−0.22	5.73	(110) to (000)	5.96/208
$MASrCl_3$	−0.21	5.58	(111) to (000)	5.80/214
$MABaCl_3$	−0.21	5.37	(111) to (000)	5.58/222

The calculated X-ray diffraction pattern of stability-improved alkaline-earth cation perovskites $MAMgCl_3$, $MACaCl_3$, and $MASrCl_3$ are shown in Figure 4a−c, and the three prominent peaks are 29.9°, 26.0°, and 27.5° (in 2θ) for $MAMgCl_3$, 32.5°, 16.1°, and 31.5° (in 2θ) for $MACaCl_3$, and 15.4°, 31.1°, and 30.2° (in 2θ) for $MASrCl_3$. These data are the reference for future syntheses and device applications. Figure 4d shows the temperature-dependent electrical conductivity of $MAPbCl_3$ and the alkaline-earth cations (Be^{2+}, Mg^{2+}, Ca^{2+}, Sr^{2+}, and Ba^{2+}) that replace lead structures. The exact values are listed in Table 3. Indeed, $MAPbCl_3$ has a theoretical electrical conductivity of 2.8 × 10^{-6} Ω $^{-1}m^{-1}$ (at 300 K), which is close to the room temperature experimental electrical conductivity of $MAPbCl_3$, which is 2.7 × 10^{-6} Ω $^{-1}$ m^{-1}.[34] Those results convince us that the DFT calculations can offer theoretical electrical conductivity values for unknown alkaline-earth cations in the replacement of lead in perovskite structure estimations. The alkaline-earth cation replacements can increase the band gap, as can be seen in Figure 3, but decrease the electrical conductivity, and $MAMgCl_3$ has the highest electrical conductivity compared to the other alkaline-earth cation perovskites in Table 3. And, the lead-free methylammonium alkaline-earth perovskites might be suitable

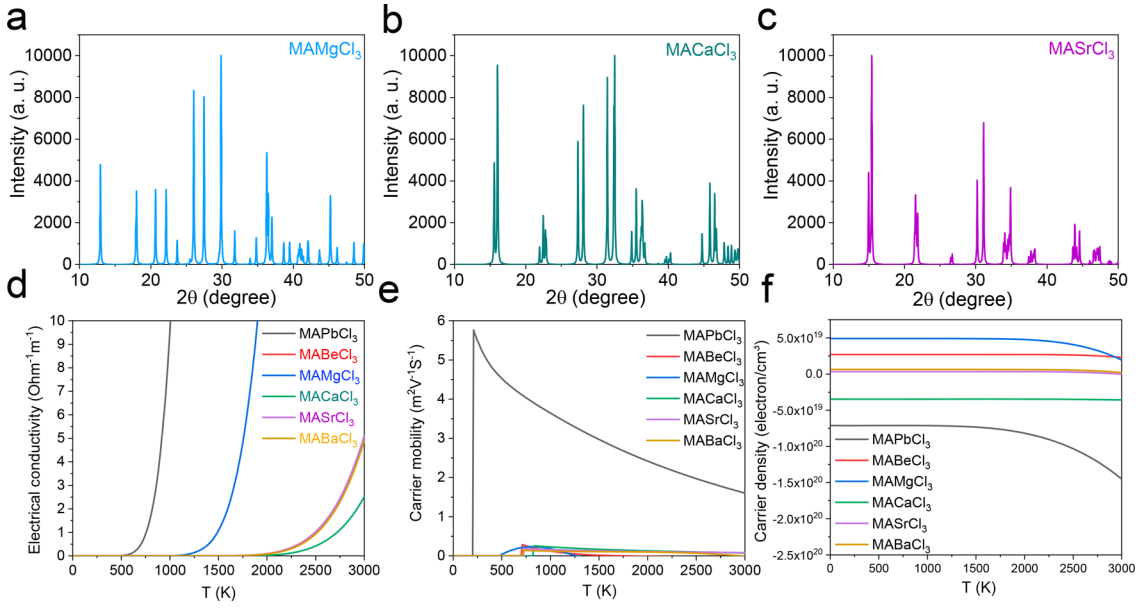

Figure 4. X-ray diffraction patterns and temperature-dependent electrical conductivity, carrier mobility, and carrier density of the alkaline-earth cation replacement structures. (a) $MAMgCl_3$ diffraction pattern. (b) $MACaCl_3$ diffraction pattern. (b) $MASrCl_3$ diffraction pattern. (d−f) Temperature-dependent electrical conductivity, carrier mobility, and carrier density of $MAPbCl_3$ and the alkaline-earth lead-free perovskite structures.

https://doi.org/10.1021/acsomega.2c01695
ACS Omega 2022, 7, 16204−16210

Table 3. Temperature-Dependent Electrical Conductivity of $MAPbCl_3$, $MABeCl_3$, $MAMgCl_3$, $MACaCl_3$, $MASrCl_3$, and $MABaCl_3$

T (K)	$MAPbCl_3$ (Ω^{-1} m^{-1})	$MABeCl_3$ (Ω^{-1} m^{-1})	$MAMgCl_3$ (Ω^{-1} m^{-1})	$MACaCl_3$ (Ω^{-1} m^{-1})	$MASrCl_3$ (Ω^{-1} m^{-1})	$MABaCl_3$ (Ω^{-1} m^{-1})
300	2.80×10^{-6}	0	0	0	0	0
400	4.86×10^{-4}	0	3.18×10^{-32}	0	0	0
500	1.15×10^{-2}	0	2.37×10^{-9}	0	0	0
600	$9.97 \times l0^{-2}$	6.40×10^{-34}	3.13×10^{-7}	0	0	5.27×10^{-36}
700	0.48	4.54×10^{-31}	1.05×10^{-5}	1.94×10^{-33}	1.95×10^{-31}	1.68×10^{-31}
800	1.64	1.55×10^{-9}	1.49×10^{-4}	5.48×10^{-31}	7.92×10^{-10}	6.52×10^{-10}
900	4.32	4.20×10^{-8}	1.19×10^{-3}	1.24×10^{-9}	2.45×10^{-8}	1.95×10^{-8}
1000	9.57	5.93×10^{-7}	6.38×10^{-3}	2.70×10^{-8}	3.84×10^{-7}	$3.00 \times l0^{-7}$

Table 4. Temperature-Dependent Carrier Mobility of $MAPbCl_3$, $MABeCl_3$, $MAMgCl_3$, $MACaCl_3$, $MASrCl_3$, and $MABaCl_3$

T (K)	$MAPbCl_3$ (cm^2 V^{-1} s^{-1})	$MABeCl_3$ (cm^2 V^{-1} s^{-1})	$MAMgCl_3$ (cm^2 V^{-1} s^{-1})	$MACaCl_3$ (cm^2 V^{-1} s^{-1})	$MASrCl_3$ (cm^2 V^{-1} s^{-1})	$MABaCl_3$ (cm^2 V^{-1} s^{-1})
300	5.20	0	0	0	0	0
400	4.81	0	0	0	0	0
500	4.53	0	0.04	0	0	0
600	0.31	0	0.14	0	0	0
700	4.12	0	0.21	0	0	0
800	3.95	0.22	0.23	0	0.18	0.13
900	3.79	0.17	0.22	0.24	0.17	0.13
1000	3.64	0.12	0.18	0.23	0.16	0.12

for high-temperature devices and applications. At 1000 K, the calculated electrical conductivities of $MAPbCl_3$, $MABeCl_3$, $MAMgCl_3$, $MACaCl_3$, $MASrCl_3$, and $MABaCl_3$ are 9.57, 5.93×10^{-7}, 6.38×10^{-3}, 2.70×10^{-8}, 3.84×10^{-7}, and 3.00×10^{-7} Ω^{-1} m^{-1}, respectively.

Figure 4e shows the temperature-dependent carrier mobility, and the values are listed in Table 4. The alkaline-earth cations that replace lead will increase the carrier mobilities within the structures. For discussing the carrier mobility deviations between experiment and calculation, the experimental carrier mobility of $MAPbCl_3$ at 300 K is 4.14 (cm^2 V^{-1} s^{-1}),[35] which is close to the calculated result (5.2 cm^2 V^{-1} s^{-1}). $MAMgCl_3$ has the highest carrier mobility within the alkaline-earth cation perovskites, namely, 0.04 cm^2 V^{-1} s^{-1} at 500 K. The most stable $MACaCl_3$ has the carrier mobility of 0.24 cm^2 V^{-1} s^{-1} at 900 K. These indicate that $MAMgCl_3$ could be applied in an ultraviolet C luminescence device with a 289 nm emission peak, and the carrier mobility might be 0.04 cm^2 V^{-1} s^{-1} under 500 K. Still, the $MACaCl_3$ device needs to operate under a higher temperature such as 900 K. Finally, this research predicts the alkaline-earth cation perovskite might be helpful according to the calculated carrier mobility. The carrier density values of $MAPbCl_3$ and alkaline-earth cation-replaced structures are shown in Figure 4f. $MAPbCl_3$ has the largest and constant carrier density (7.2×10^{19} electron/cm^3) below 1500 K, and the same trend occurs with $MAMgCl_3$ with lower carrier density (5×10^{19} electron/cm^3). $MACaCl_3$ and $MABeCl_3$ have much lower amounts (3.5×10^{19} and 2.75×10^{19} electron/cm^3) with opposite signs. On the contrary, $MASrCl_3$ and $MABaCl_3$ have nearly zero. And, the results show that $MAPbCl_3$, $MAMgCl_3$, and $MASrCl_3$ are n-type semiconductors with the electron as the dominant carrier. $MABeCl_3$, $MACaCl_3$, and $MABaCl_3$ are p-type semiconductors with the hole as the dominant carrier with negative carrier (electron) density.

CONCLUSIONS

This research tries to determine the possibility of the alkaline-earth cation perovskite as a potential lead-free ultrawide band-gap perovskite material according to the calculated dynamic structure stability, electrical conductivity, and carrier mobility. The Mg^{2+}, Ca^{2+}, and Sr^{2+} cation replacements of Pb^{2+} cation could improve the dynamic stability by reducing the imaginary part of the phonon DOSs. $MACaCl_3$ is the most dynamically stable alkaline-earth cation perovskite; it not only has a Goldschmidt factor of 0.96 (lower deviation than 1) but also has the imaginary part phonon DOS of 0%. Our results point out that the imaginary part of phonon DOS could be a factor in evaluating the crystal stability of perovskite. The DFT calculation results of $MAPbCl_3$ perovskite structures have calculated electrical conductivity and carrier mobility results close to the experiment results. Hence, the $MACaCl_3$ structure could be predicted with a 5.96 eV band gap and with the electrical conductivity and carrier mobility as 1.24×10^{-9} Ω^{-1} m^{-1} and 0.24 cm^2 V^{-1} S^{-1}, respectively, at 900 K. Our calculation results shows that the $MACaCl_3$ is a dynamic stable structure and could be a candidate for ultrawide band-gap high-temperature applications in the future.

METHODS

The density functional theory calculations are processed by Vienna ab initio Simulation Package (VASP),[36−38] and different exchange-correlation functionals (GGA-PBE and sx-LDA) are chosen. The structural optimization is set up with a default plane-wave cutoff energy of 520 eV; the requested k-spacing is 0.2 per angstrom, which leads to a $6 \times 6 \times 6$ mesh, and we are using first-order Methfessel-Paxton smearing with a width of 0.2 eV. Typically, the percentage of volume change from the original input cell toward the structural optimization cell is less than 20%. Then, the optimized structures were calculated by the functional of sx-LDA for a discussion of other electronic band structures. The calculation is set with $6 \times 6 \times 6$ k-spacing mesh and Gaussian smearing width of 0.05 eV. The phonon and related calculations were processed by GGA-PBE, with the plane-wave cutoff of 500 eV and k-spacing of $5 \times 5 \times 5$ mesh, and the Methfessel-Paxton smearing width was set as 0.2 eV. The semiconductor properties (electrical conductivity, carrier

https://doi.org/10.1021/acsomega.2c01695
ACS Omega 2022, 7, 16204−16210

mobility, and carrier density) were calculated within Boltzmann's transport theory, processed by GGAPBE, applying BoltzTraP based on the k-mesh and bands used for the Fermi surface above, with the chemical potential setting at 11 mu within 26 functions. The X-ray diffraction pattern calculation used the software Mercury.

■ ASSOCIATED CONTENT

Supporting Information

The Supporting Information is available free of charge at https://pubs.acs.org/doi/10.1021/acsomega.2c01695.

Additional material for the complete electronic, phonon, and crystal information of this study (PDF)

■ AUTHOR INFORMATION

Corresponding Author

Chih Shan Tan − *Institute of Electronics, National Yang Ming Chiao Tung University, Hsinchu 30010, Taiwan;* orcid.org/0000-0001-9043-3237; Email: cstan@nycu.edu.tw

Author

Chung Chi Yang − *Institute of Electronics, National Yang Ming Chiao Tung University, Hsinchu 30010, Taiwan*

Complete contact information is available at: https://pubs.acs.org/10.1021/acsomega.2c01695

Notes

The authors declare no competing financial interest.

■ ACKNOWLEDGMENTS

This work was funded by the Ministry of Science and Technology of Taiwan (Grant Nos. MOST 110-2636-E-009-020 and MOST 111-2636-E-A49-002).

■ REFERENCES

(1) Guo, W.; Sun, H.; Torre, B.; Li, J.; Sheikhi, M.; Jiang, J.; Li, H.; Guo, S.; Li, K.-H.; Lin, R.; Giugni, A.; Di Fabrizio, E.; Li, X.; Ye, J. Lateral-Polarity Structure of AlGaN Quantum Wells: A Promising Approach to Enhancing the Ultraviolet Luminescence. *Adv. Funct. Mater.* **2018**, *28* (32), 1802395.

(2) Jeon, K.-J.; Lee, Z.; Pollak, E.; Moreschini, L.; Bostwick, A.; Park, C.-M.; Mendelsberg, R.; Radmilovic, V.; Kostecki, R.; Richardson, T. J.; Rotenberg, E. Fluorographene: a wide bandgap semiconductor with ultraviolet luminescence. *ACS Nano* **2011**, *5* (2), 1042−1046.

(3) Li, S.; Zhang, Y.; Yang, W.; Liu, H.; Fang, X. 2D Perovskite $Sr_2Nb_3O_{10}$ for High-Performance UV Photodetectors. *Adv. Mater.* **2020**, *32* (7), e1905443.

(4) Luo, Y.; Hu, Y.; Xie, Y. Highly polarization-sensitive, visible-blind and self-powered ultraviolet photodetection based on two-dimensional wide bandgap semiconductors: a theoretical prediction. *J. Mater. Chem. A* **2019**, *7* (48), 27503−27513.

(5) Shi, H.; An, Z. Ultraviolet afterglow. *Nature Photon* **2019**, *13* (2), 74−75.

(6) Cai, P.; Huang, Y.; Seo, H. J. Anti-Stokes Ultraviolet Luminescence and Exciton Detrapping in the Two-Dimensional Perovskite $(C_6H_5C_2H_4NH_3)_2PbCl_4$. *J. Phys. Chem. Lett.* **2019**, *10* (14), 4095−4102.

(7) Wang, W.; Zhao, D.; Zhang, F.; Li, L.; Du, M.; Wang, C.; Yu, Y.; Huang, Q.; Zhang, M.; Li, L.; Miao, J.; Lou, Z.; Shen, G.; Fang, Y.; Yan, Y. Highly Sensitive Low-Bandgap Perovskite Photodetectors with Response from Ultraviolet to the Near-Infrared Region. *Adv. Funct. Mater.* **2017**, *27* (42), 1703953.

(8) Zhang, Y.; Cheng, X.; Tu, D.; Gong, Z.; Li, R.; Yang, Y.; Zheng, W.; Xu, J.; Deng, S.; Chen, X. Engineering the Bandgap and Surface Structure of $CsPbCl_3$ Nanocrystals to Achieve Efficient Ultraviolet Luminescence. *Angewandte Chemie (International ed. in English)* **2021**, *60* (17), 9693−9698.

(9) Tan, C. S.; Hou, Y.; Saidaminov, M. I.; Proppe, A.; Huang, Y. S.; Zhao, Y.; Wei, M.; Walters, G.; Wang, Z.; Zhao, Y.; Todorovic, P.; Kelley, S. O.; Chen, L. J.; Sargent, E. H. Heterogeneous Supersaturation in Mixed Perovskites. *Advanced science (Weinheim, Baden-Wurttemberg, Germany)* **2020**, *7* (7), 1903166.

(10) Gong, X.; Guan, L.; Pan, H.; Sun, Q.; Zhao, X.; Li, H.; Pan, H.; Shen, Y.; Shao, Y.; Sun, L.; Cui, Z.; Ding, L.; Wang, M. Highly Efficient Perovskite Solar Cells via Nickel Passivation. *Adv. Funct. Mater.* **2018**, *28* (50), 1804286.

(11) Ren, H.; Yu, S.; Chao, L.; Xia, Y.; Sun, Y.; Zuo, S.; Li, F.; Niu, T.; Yang, Y.; Ju, H.; Li, B.; Du, H.; Gao, X.; Zhang, J.; Wang, J.; Zhang, L.; Chen, Y.; Huang, W. Efficient and stable Ruddlesden-Popper perovskite solar cell with tailored interlayer molecular interaction. *Nat. Photonics* **2020**, *14* (3), 154−163.

(12) Zhai, Y.; Baniya, S.; Zhang, C.; Li, J.; Haney, P.; Sheng, C.-X.; Ehrenfreund, E.; Vardeny, Z. V. Giant Rashba splitting in 2D organic-inorganic halide perovskites measured by transient spectroscopies. *Science advances* **2017**, *3* (7), e1700704.

(13) Colmenero, F.; Fernández, A. M.; Cobos, J.; Timón, V. Periodic DFT Study of the Thermodynamic Properties and Stability of Schoepite and Metaschoepite Mineral Phases. *ACS Earth Space Chem.* **2019**, *3* (1), 17−28.

(14) Colmenero, F.; Fernández, A. M.; Timón, V.; Cobos, J. Becquerelite mineral phase: crystal structure and thermodynamic and mechanical stability by using periodic DFT. *RSC Adv.* **2018**, *8* (43), 24599−24616.

(15) Tan, C.-S.; Huang, M. H. Metal-like Band Structures of Ultrathin Si {111} and {112} Surface Layers Revealed through Density Functional Theory Calculations. *Chemistry (Weinheim an der Bergstrasse, Germany)* **2017**, *23* (49), 11866−11871.

(16) Tan, C.-S.; Huang, M. H. Density Functional Theory Calculations Revealing Metal-like Band Structures for Ultrathin Germanium (111) and (211) Surface Layers. *Chemistry, an Asian journal* **2018**, *13*, 1972.

(17) Tan, C.-S.; Huang, M. H. Density Functional Theory Calculations Revealing Metal-like Band Structures and Work Function Variation for Ultrathin Gallium Arsenide (111) Surface Layers. *Chemistry, an Asian journal* **2019**, *14* (13), 2316−2321.

(18) Tan, C.-S.; Chen, H.-S.; Chiu, C.-Y.; Wu, S.-C.; Chen, L.-J.; Huang, M. H. Facet-Dependent Electrical Conductivity Properties of PbS Nanocrystals. *Chem. Mater.* **2016**, *28* (5), 1574−1580.

(19) Tan, C.-S.; Chen, Y.-J.; Hsia, C.-F.; Huang, M. H. Facet-Dependent Electrical Conductivity Properties of Silver Oxide Crystals. *Chemistry, an Asian journal* **2017**, *12* (3), 293−297.

(20) Tan, C.-S.; Hsu, S.-C.; Ke, W.-H.; Chen, L.-J.; Huang, M. H. Facet-dependent electrical conductivity properties of Cu_2O crystals. *Nano Lett.* **2015**, *15* (3), 2155−2160.

(21) Tan, C.-S.; Lu, Y.-J.; Chen, C.-C.; Liu, P.-H.; Gwo, S.; Guo, G.-Y.; Chen, L.-J. Magnetic MoS_2 Interface Monolayer on a CdS Nanowire by Cation Exchange. *J. Phys. Chem. C* **2016**, *120* (40), 23055−23060.

(22) Jacobs, R.; Luo, G.; Morgan, D. Materials Discovery of Stable and Nontoxic Halide Perovskite Materials for High-Efficiency Solar Cells. *Adv. Funct. Mater.* **2019**, *29* (23), 1804354.

(23) Lee, B. D.; Park, W. B.; Lee, J.-W.; Kim, M.; Pyo, M.; Sohn, K.-S. Discovery of Lead-Free Hybrid Organic/Inorganic Perovskites Using Metaheuristic-Driven DFT Calculations. *Chem. Mater.* **2021**, *33* (2), 782−798.

(24) Lu, S.; Zhou, Q.; Ouyang, Y.; Guo, Y.; Li, Q.; Wang, J. Accelerated discovery of stable lead-free hybrid organic-inorganic perovskites via machine learning. *Nat. Commun.* **2018**, *9* (1), 3405.

(25) Tao, Q.; Xu, P.; Li, M.; Lu, W. Machine learning for perovskite materials design and discovery. *npj Comput. Mater.* **2021**, *7* (1). DOI: 10.1038/s41524-021-00495-8.

(26) Perdew, J. P.; Burke, K.; Ernzerhof, M. Generalized Gradient Approximation Made Simple. *Physical review letters* **1996**, *77* (18), 3865−3868.

(27) Bylander, D. M.; Kleinman, L. Good semiconductor band gaps with a modified local-density approximation. *Phys. Rev. B* **1990**, *41* (11), 7868−7871.
(28) Seidl, A.; Gorling, A.; Vogl, P.; Majewski, J. A.; Levy, M. Generalized Kohn-Sham schemes and the band-gap problem. *Phys. Rev. B* **1996**, *53* (7), 3764−3774.
(29) Al Ghaithi, A. O.; Aravindh, S. A.; Hedhili, M. N.; Ng, T. K.; Ooi, B. S.; Najar, A. Optical Properties and First-Principles Study of $CH_3NH_3PbBr_3$ Perovskite Structures. *ACS Omega* **2020**, *5* (21), 12313−12319.
(30) Bhaumik, S. Exciton Relaxation Dynamics in Perovskite Cs_4PbBr_6 Nanocrystals. *ACS Omega* **2020**, *5* (35), 22299−22304.
(31) Ghaithan, H. M.; Alahmed, Z. A.; Qaid, S. M. H.; Hezam, M.; Aldwayyan, A. S. Density Functional Study of Cubic, Tetragonal, and Orthorhombic $CsPbBr_3$ Perovskite. *ACS Omega* **2020**, *5* (13), 7468−7480.
(32) López, C. A.; Abia, C.; Alvarez-Galván, M. C.; Hong, B.-K.; Martínez-Huerta, M. V.; Serrano-Sánchez, F.; Carrascoso, F.; Castellanos-Gómez, A.; Fernández-Díaz, M. T.; Alonso, J. A. Crystal Structure Features of $CsPbBr_3$ Perovskite Prepared by Mechanochemical Synthesis. *ACS Omega* **2020**, *5* (11), 5931−5938.
(33) Pazoki, M.; Jacobsson, T. J.; Hagfeldt, A.; Boschloo, G.; Edvinsson, T. Effect of metal cation replacement on the electronic structure of metalorganic halide perovskites: Replacement of lead with alkaline-earth metals. *Phys. Rev. B* **2016**, *93* (14). DOI: 10.1103/PhysRevB.93.144105.
(34) Maculan, G.; Sheikh, A. D.; Abdelhady, A. L.; Saidaminov, M. I.; Haque, M. A.; Murali, B.; Alarousu, E.; Mohammed, O. F.; Wu, T.; Bakr, O. M. $CH_3NH_3PbCl_3$ Single Crystals: Inverse Temperature Crystallization and Visible-Blind UV-Photodetector. *J. Phys. Chem. Lett.* **2015**, *6* (19), 3781−3786.
(35) Hsu, H.-P.; Li, L.-C.; Shellaiah, M.; Sun, K. W. Structural, Photophysical, and Electronic Properties of $CH_3NH_3PbCl_3$ Single Crystals. *Sci. Rep.* **2019**, *9* (1), 13311.
(36) Kresse, G.; Hafner, J. Ab initio molecular dynamics for liquid metals. *Phys. Rev. B* **1993**, *47* (1), 558−561.
(37) Kresse, G.; Furthmuller, J. Efficient iterative schemes for ab initio total-energy calculations using a plane-wave basis set. *Phys. Rev. B* **1996**, *54* (16), 11169−11186.
(38) Kresse, G.; Furthmüller, J. Efficiency of ab-initio total energy calculations for metals and semiconductors using a plane-wave basis set. *Comput. Mater. Sci.* **1996**, *6* (1), 15−50.

https://doi.org/10.1021/acsomega.2c01695
ACS Omega 2022, 7, 16204−16210